Flow of wormlike micellar fluids around a sharp bend: Effects of branching and shear-banding

Yiran Zhang,[1] Hadi Mohammadigoushki,[2] Margaret Y. Hwang,[1,*] and Susan J. Muller[1,†]
[1]*Department of Chemical and Biomolecular Engineering, University of California, Berkeley, California 94720, USA*
[2]*Department of Chemical and Biomedical Engineering, FAMU-FSU College of Engineering, Tallahassee, Florida 32310, USA*

(Received 29 April 2018; published 4 September 2018)

The flow of wormlike micellar solutions around a 90° sharp microfluidic bend was studied using rheometry, flow visualization, and velocimetry. By carefully choosing the composition of the test solutions, all four combinations of linear or branched micelles and shear-banding or non-shear-banding solutions were accessed using four wormlike micellar solutions. The flow behavior of the solutions was examined in similar conditions of about $1 < Wi < 300$ and $10^{-6} < Re < 10^{-2}$. When comparing the flow around the microbend of the two shear-banding solutions with the two non-shear-banding ones, the secondary flows showed distinct differences at about $10 < Wi < 100$. Flow visualization showed that a steady lip vortex formed at the inner upstream corner of the microbend in the non-shear-banding solutions, while a lip (inner upstream corner) vortex and an outer corner vortex formed in the shear-banding solutions. On the other hand, when comparing the solutions with similar rheological characteristics but different micelle morphology (linear versus branched), no significant differences in the flow behavior were observed. These results suggest that shear-banding plays a central role in determining the secondary flow behavior around the microbend, while the effect of micelle morphology is minimal for wormlike micelle solutions. Additional particle tracking velocimetry measurements were carried out both upstream of and around the microbend. The resulting velocity profiles in the shear-banding solutions show marked disagreement with calculations based on the shear-rate-dependent apparent viscosity using the Carreau model. These results suggest that the shear-banding effect on the flow around the microbend could be correlated to the development of a "jetting" flow regime upstream of the bend, which could be a result of the nonmonotonic stress – shear rate relationship in shear-banding wormlike micellar solutions.

DOI: 10.1103/PhysRevFluids.3.093301

I. INTRODUCTION

Understanding the flow of complex fluids in microfluidic devices is essential to achieving optimized designs for lab-on-a-chip systems. In addition, microfluidic devices provide a unique opportunity to study high elasticity flows. One can easily generate elastically dominated flows in these miniaturized devices, since the ratio of elastic to inertial forces scales as $1/L^2$, where L is the characteristic length scale of the device [1]. For this reason, microfluidic experiments have provided a useful platform for studies of purely elastic instabilities that are driven by a coupling between streamline curvature and elastic hoop stresses due to streamwise tension. Recent

*Current address: The Dow Chemical Company, Midland, Michigan 48686, USA.
†Corresponding author: muller2@berkeley.edu

studies have included elucidation of viscoelastic instabilities in flows through microcontraction and microexpansion geometries [1–12], in cross slot geometries [13–21], in serpentine channels [22–25], and in T junctions [26].

Flow around a sharp 90° bend is a shear dominated flow that occurs in many microfluidic devices. However, very few studies of viscoelastic flows around a sharp 90° bend appear in the literature. Early numerical simulations performed for two-dimensional, steady flow in a sharp bend indicate that at low Reynolds number, increasing elasticity leads to only modest deviations from the Newtonian flow, with a slight shift of the streamlines towards the outer wall [27,28]. Among the first experiments are those of Cochrane *et al.* [29], who examined a constant viscosity, highly elastic aqueous solution of polyacrylamide (PAA) in a channel of a rectangular cross section that was 1.2-cm wide and 2.0-cm deep. At Reynolds numbers of 4 and 16 and Weissenberg numbers of 0.03 and 0.14, negligible changes in the streamlines relative to the Newtonian flow were observed. Here, Reynolds number was defined as $Re = \rho U w/\eta_0$ and Weissenberg number was defined as $Wi = \lambda U/w$, where ρ, U, w, η_0, and λ are the fluid density, mean velocity, channel width, zero-shear-rate viscosity, and fluid relaxation time, respectively. Chono and Iemoto [28] subsequently considered a shear-thinning, viscoelastic aqueous solution of PAA in a sharp bend with a cross section of width 5.0 cm and a depth of 25.0 cm. These authors explored $0.47 < Re < 9.06$ and $1.10 < Wi < 1.97$, where both Re and Wi were based on the shear-rate dependent viscosity and relaxation time, and reported a slight shift in the streamlines relative to a Newtonian fluid, but no secondary flow. Chono and Iemoto [28] did, however, observe a small vortex at the inside, upstream corner of the bend when the width of the downstream channel was made significantly smaller than that of the upstream channel for this same range of Re and Wi.

Gulati *et al.* [30] reported an elastic lip vortex in a sharp microbend when the upstream and downstream channels are of equal width. Gulati *et al.* [30] studied a highly shear-thinning aqueous solution of λ-DNA in a sharp bend with a cross section 200-μm wide and 225-μm deep. The small dimensions of the device allowed very low Re ($10^{-6} < Re < 10^{-2}$) and very high Wi ($0.42 < Wi < 126$) to be probed. A steady "lip" vortex appears at the inner, upstream corner of the bend at Wi (based on the longest Maxwell relaxation time) of 0.84. This vortex grows in size with further increases in Wi but the flow remains steady and time-independent for all $Wi > 0.84$. In a subsequent study, Gulati *et al.* [31] performed additional experiments in the same geometry with a dilute and a semi-dilute aqueous solution of poly(ethylene oxide) (PEO). The dilute PEO solution was essentially non-shear-thinning, while the semi-dilute PEO solution was moderately shear-thinning. For the shear-thinning PEO solution, dynamics similar to those in the DNA solution were reported: a steady lip vortex formed and grew in size for $Wi > 3.54$. However, the vortex was absent for the dilute, non-shear-thinning PEO solution for the entire range of conditions probed ($3.3\times10^{-4} < Re < 1.6\times10^{-2}$ and $1.1 < Wi < 52.8$). Thus, shear-thinning appears central to the formation and growth of the elastic lip vortex in flow around a sharp bend.

More recently, Hwang *et al.* [32] examined the flow of two wormlike micelle solutions in flow around a sharp microbend. Two solutions of cetylpyridinium chloride (CPCl) and sodium salicylate (NaSal) with different salt-to-surfactant ratios R were studied. One solution, with $R = [\text{NaSal}]/[\text{CPCl}] = 0.55$, consisted of linear wormlike micelles and was shear-thinning but non-shear-banding; the second solution, with $R = 0.79$, consisted of branched wormlike micelles and was shear-thinning and shear-banding. With increasing Wi, the linear, non-shear-banding solution displays a steady lip vortex that grows in size for $Wi \geqslant 6$, however, as Wi reaches approximately 20, the vortex becomes time dependent and fluctuates in length for the remainder of the Wi range that was accessed (i.e., $20 < Wi < 400$). Hwang *et al.* [32] did not observe this second transition, from a steady lip vortex to a fluctuating, time-dependent lip vortex, with a shear-thinning PEO solution similar to the one used in Gulati *et al.* [31], despite accessing comparably high Wi for the solutions. The branched, shear-banding wormlike micelle solution exhibited two different transitions with increasing Wi over this same range. A first transition at $Wi = 4$ was characterized by the appearance of two intermittent vortices, one at the lip and one at the far outside corner. For $Wi > 160$, a second transition was noted, to a flow characterized by only a fluctuating lip vortex.

TABLE I. Shear rheology of the wormlike micelle solutions (T = 22.5 °C).

Solution		Shear	Micelle	Maxwell model		Carreau model		
[CpCl] (mM)	R = [NaSal]/[CpCl]	banding?	morphology	G_0 [Pa]	λ [s]	η_0[Pas]	λ_c[s]	n
95	0.55	N	Linear	8.29	0.59	5.73	0.83	0.20
95	0.57	Y	Linear	14.16	1.09	19.04	1.74	0.021
95	0.79	Y	Branched	34.61	0.52	18.69	0.64	0
25	1	N	Branched	2.52	1.50	3.66	1.83	0.23

The differences between these transitions in flow around a bend may arise from a number of sources. Here, we focus on the roles of branching and shear-banding. We have identified two additional solutions of CpCl and NaSal for this study. The first solution contains the same concentration of CPCl as in the earlier study, but by subtly varying the salt-to-surfactant ratio (to $R = 0.57$) we obtain a solution of linear wormlike micelles that displays shear-banding. The second solution consists of a lower concentration of CPCl but a higher salt ratio and contains branched wormlike micelles but is non-shear-banding. We have also re-run the earlier experiments with the linear, non-shear-banding system and the branched, shear-banding system of CPCl/NaSal. Thus, we hope to elucidate the extent to which branching and shear-banding affect the flow transitions observed in flow around a sharp microbend.

II. MATERIALS AND METHODS

The wormlike micellar solutions were studied in a silicon-based microfluidic device with a sharp bend. The device consists of two rectangular channels meeting at a 90° angle. Both channels are 110-μm wide, 55-μm deep, and 6-mm long from the bend to the fluid reservoirs. The device was fabricated using deep reactive ion etching, and sealed by anodically bonding a Pyrex glass wafer to the silicon device. More detailed descriptions of the microfluidic device and the fabrication process can be found elsewhere [3,32].

Flows of four wormlike micellar solutions based on CPCl and NaSal were explored in the 90° microbend geometry. Both chemicals were from Spectrum Chemical and used as received. The surfactant concentration [CpCl] and the salt-to-surfactant concentration ratio, R = [NaSal]/[CpCl], of the four tested solutions are listed in Table I. The concentrations of these four solutions are chosen so that they cover two different wormlike micelle morphologies (linear and branched) as well as two different nonlinear rheological characteristics (shear-banding and non-shear-banding). The properties of the solutions are discussed in detail in Section 3. All the solutions were prepared in filtered deionized water, and they were seeded with 1-μm green fluorescent polystyrene particles (Fluoro-Max) at 0.005 vol% for flow visualization. The rheological properties of the solutions are not affected by the seeding particles at this concentration.

The flow in the microbend was controlled by a syringe pump (Harvard PHD2000) and 2.5-mL glass syringes (Hamilton Gastight). Volumetric flow rates tested ranged from 2.5- to 500-μL/hr, and each flow rate was maintained for at least 30 min before visualization to ensure steady-state behavior. The experiments were carried out at room temperature, which was monitored to be fluctuating between 21.5 and 22.5 °C. The flow visualization was carried out using a Leica DMIRE2 inverted microscope with a 20x/0.5 NA objective and external light source (Leica EL6000). The microscope was focused at the midplane of the microfluidic channel. Images were captured using a high-speed camera (Vision Research, Phantom Miro M310) with a frame rate between 24 and 1000 fps. Streak images of the flow were obtained using Matlab by overlaying frames from a stack of 20–2000 frames captured at 24 fps.

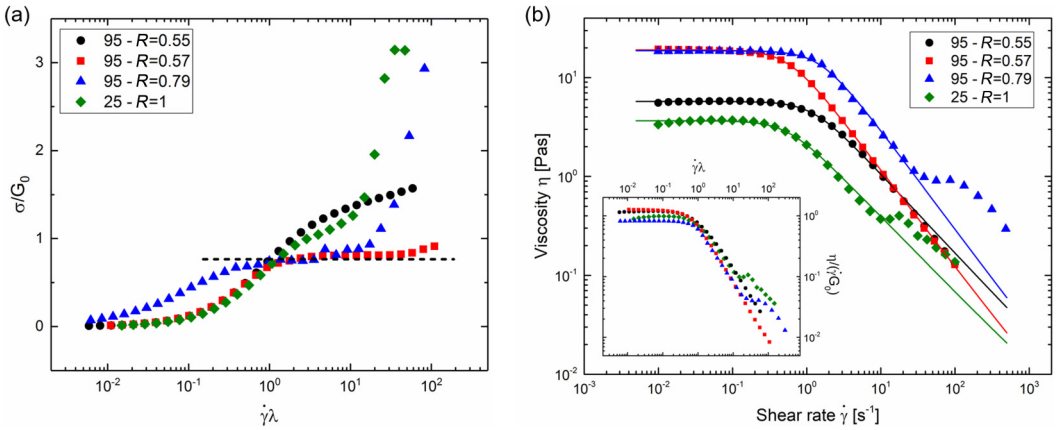

FIG. 1. Steady shear rheological characterization of the four solutions used in this study.

As the seeding concentration of the tracer particles was optimized for flow visualization and streak imaging, the particle density in high-speed images was not sufficient for reliable particle image velocimetry (PIV) measurements. Instead, a particle tracking velocimetry (PTV) scheme was used to obtain information on the fluid velocity field in the microbend geometry. Based on the flow rate, different recording speeds (60–1000 fps) were used to record a stack of frames (up to 10 000 frames). Particle trajectories were tracked using MOSAIC open source plugin in ImageJ [33] and further analyzed in Matlab with specially written codes. This PTV protocol allowed us to carry out velocity field measurements similar to particle imaging velocimetry [34] and compare the velocity profiles in the straight part of the channel with theoretical predictions. The detailed protocol and calibrations using Newtonian fluids are described in the supplementary material [35].

III. FLUID CHARACTERIZATION

The rheology of the test solutions was characterized using a stress-controlled rheometer (Malvern-Gemini). All measurements were carried out at 22.5 °C, using a Couette geometry (inner cylinder diameter 25 mm and outer cylinder diameter 27 mm). Small amplitude oscillatory shear (SAOS) measurements show that, in all four wormlike micellar solutions, the storage and loss moduli, G' and G'', are in good agreement with a single-mode Maxwell model (see supplementary Figure S1 [35]). Slight deviations from the Maxwell model are observed at high shear rates, which is well-known for wormlike micellar solutions [36]. The relaxation times λ and plateau moduli G_0 obtained with this model fitting are listed in Table I. The four test solutions have similar Maxwell relaxation times (around 1 s), which in the bend flow experiments allowed access to a similar range of Weissenberg number and therefore meaningful comparisons between test solutions.

The results from steady shear measurements are shown in Figure 1. In Fig. 1(a), the shear stress and shear rate are normalized by G_0 and λ, respectively. In solutions with [CpCl] = 95 mM and R = [NaSal]/[CpCl] = 0.57 (referred to as 95 mM-R = 0.57 herein), as well as 95 mM-R = 0.79, shear stress plateaus are observed, as indicated by the dashed horizontal line. The plateaus are at approximately $\sigma/G_0 \approx 1$ and start at the dimensionless shear rate $\dot{\gamma}\lambda \approx 1$. Such shear stress plateaus are a signature of shear-banding in steady shear measurements. In comparison, the other two solutions, 95 mM-R = 0.55 and 25 mM-R = 1 do not exhibit a stress plateau; instead the shear stresses increase monotonically with increasing shear rate. Therefore, these two solutions are non-shear-banding in steady shear flow.

Figure 1(b) shows the apparent viscosity as a function of shear rate. All four solutions show significant shear thinning from about $\dot{\gamma}\lambda > 1$ [see Fig. 1(b) inset]. The shear-rate-dependent-viscosities

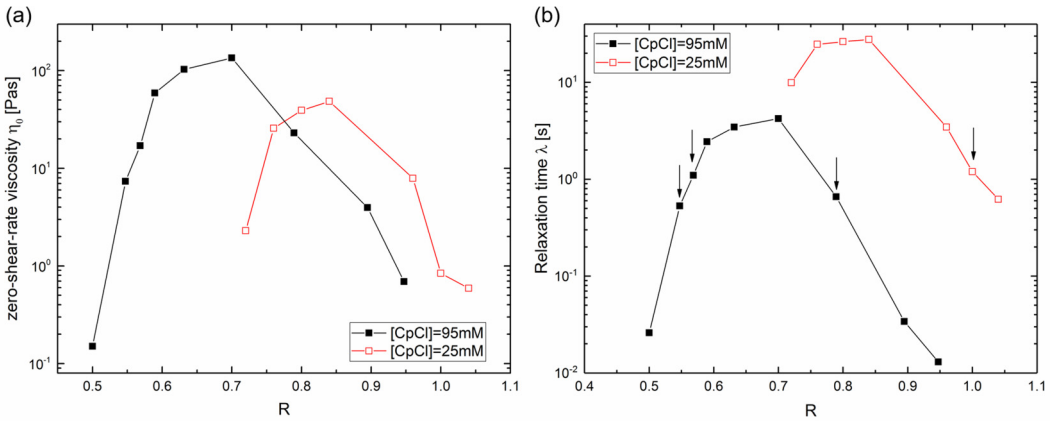

FIG. 2. Effect of salt-to-surfactant ratio R on (a) zero-shear-rate viscosity and (b) relaxation time of the solution. Solutions on the left side of the maxima contain linear micelles, while on the right side contain branched micelles. Arrows in (b) indicate the solutions used in this study.

are fitted using the Carreau model:

$$\eta(\dot{\gamma}) = \eta_\infty + (\eta_0 - \eta_\infty)[1 + (\lambda_c \dot{\gamma})^2]^{\frac{n-1}{2}}, \tag{1}$$

where η_0 is the zero shear rate viscosity, η_∞ is the infinite shear rate viscosity (fixed as the viscosity of water), n is the power-law index, and λ_c is the Carreau relaxation time. The model fitting is shown as solid lines in Fig. 1(b), and the fitting parameters are also listed in Table I. In the two shear-banding solutions, 95 mM-$R = 0.57$ and $R = 0.79$, the power-law indices n obtained from the Carreau model fit are close to 0, which is expected given the stress plateau in Fig. 1(a). These parameters are used in the microbend experiments to calculate the shear-rate-dependent viscosity, $\eta(\dot{\gamma})$, and are also used to calculate the theoretical velocity profiles across the width of the straight channel for comparisons with experimentally measured profiles. The rheology of two solutions, 95 mM-$R = 0.55$ and 95 mM-$R = 0.79$, was in agreement with previous characterization using a cone-and-plate geometry by Hwang *et al.* [32]. The first normal stress coefficient as a function of shear rate for these two fluids is available in Figure 4 of reference [32] for a limited range of shear rates.

It is worth noting that in two of the test solutions, 95 mM-$R = 0.79$ and 25 mM-$R = 1$, deviations from the Carreau model fit can be seen at high shear rates (about $\dot{\gamma} > 10 - 100\,\mathrm{s}^{-1}$), where the two solutions exhibit shear thickening behavior. This can be attributed to shear-induced structure formation in these wormlike micellar systems [37]. The detailed rheological characterization of the shear thickening regime is difficult in the current rheometry setup, as the high rotational speed of the Couette cylinder required to reach these high shear rates also results in significant rod-climbing, edge fracture, and air entrainment. On the other hand, in the microbend experiments presented below, we found no significant difference in the qualitative flow behavior (Wi at onset of the transition, secondary flow pattern) between shear-thickening and non-shear-thickening solutions. Therefore in this paper, we focus our attention on other rheological characteristics (e.g., shear-banding) and their effects on the flow around the microbend.

It has been well-documented that the wormlike micelle morphology changes with varying concentration of added salt [38,39]. As $R = [\mathrm{salt}]/[\mathrm{surfactant}]$ increases, the wormlike micelles transition from linear to branched. One of the rheological signatures of this transition is that the zero-shear-rate viscosity, η_0, and the relaxation time, λ, both reach maximum values [40]. Therefore, the morphology of the wormlike micelles in the four test solutions used in this study can be determined by constructing $\eta_0(R)$ and $\lambda(R)$ for a series of wormlike micelle solutions with [CpCl] = 95 mM and 25mM, as shown in Fig. 2. The points corresponding to the four test solutions are indicated with arrows in Fig. 2(b). The two solutions to the left of the maxima (95 mM-$R = 0.55$ and R = 0.57)

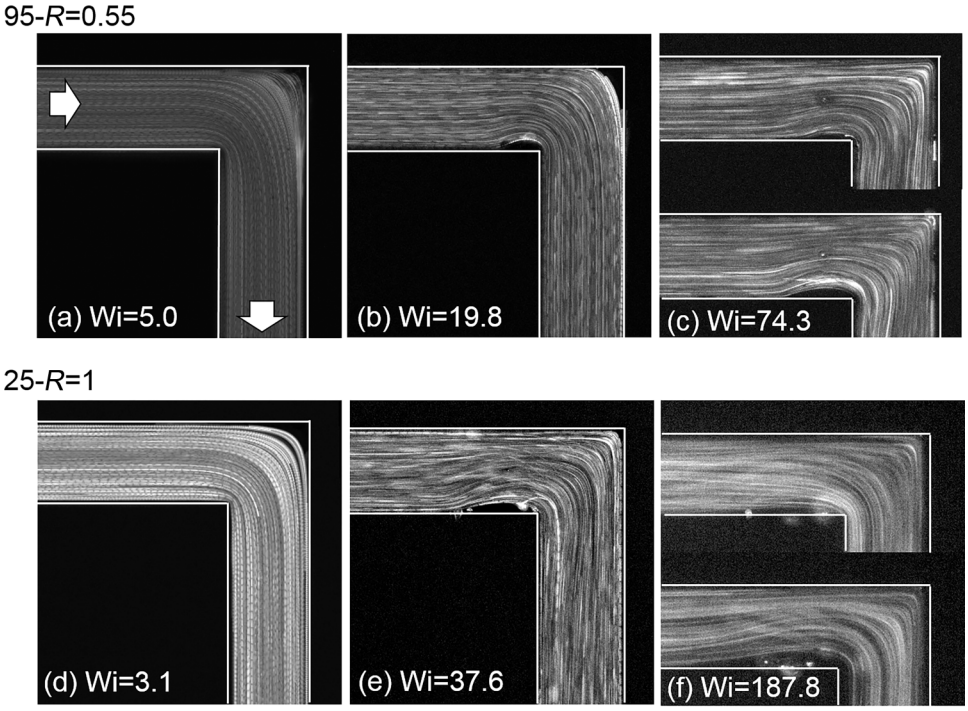

FIG. 3. Flow visualization images showing the progression of flows for the two non-shear-banding solutions. Top [(a),(b),(c)]: images show three flow regimes for the 95-$R = 0.55$ solution, which consists of linear wormlike micelles. Bottom [(d),(e),(f)]: images for the 25-$R = 1$ solution, which consists of branched wormlike micelles.

contain linear wormlike micelles, and the two that fall to the right of the maxima (95 mM-$R = 0.79$ and 25 mM-$R = 1$) contain branched micelles.

Previous work by Hwang *et al.* [32] found marked flow behavior differences in the microbend between a linear wormlike micelle solution and a branched one. However, in addition to differences in micelle morphology, the nonlinear rheological properties of the two solutions were also different: one was shear-banding, and the other was non-shear-banding. In the present study, in addition to the two solutions studied before (95 mM-$R = 0.55$ and $R = 0.79$), two more solutions (95 mM-$R = 0.57$ and 25 mM-$R = 1$) are examined, covering all four possible combinations of shear-banding and micelle morphology. This allows us to tease apart the roles played by these two factors in flow behavior in the microbend geometry.

IV. RESULTS AND DISCUSSION OF MICROBEND EXPERIMENTS

In this section the results of the microbend experiments are presented in terms of Weissenberg number, $Wi = \lambda\dot{\gamma}_c$, and Reynolds number, $Re = \rho U D_h/\eta(\dot{\gamma}_c)$, where the characteristic shear rate in the microfluidic device is given by the average fluid velocity divided by the channel half width, i.e., $\dot{\gamma}_c = 2U/w$, and $D_h = 2wh/(w+h)$ is the hydraulic diameter of the channel [3,30–32]. The Maxwell relaxation times obtained from SAOS measurements were used as λ, and $\eta(\dot{\gamma}_c)$ was calculated using the Carreau parameters obtained from steady shear measurements. We note that at the higher shear rates and *Wi* considered, the Carreau fits are extrapolated up to a decade or more beyond the maximum shear rate where we could obtain the rheological data shown in Fig. 1(b).

Representative streak images in the two non-shear-banding solutions are shown in Fig. 3. Three distinct flow regimes can be recognized for both solutions. The flows are steady, and no secondary flow was observed at low *Wi* [Figs. 3(a) and 3(d)]. As *Wi* increases, a lip vortex develops at the

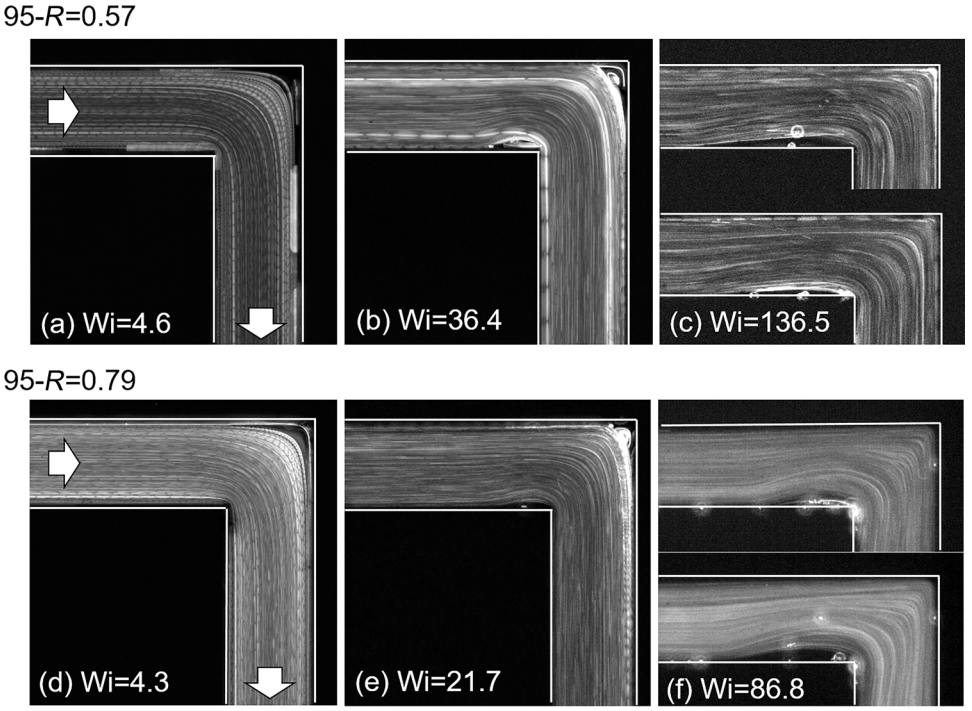

FIG. 4. Flow visualization images showing the progression of flows for the two shear-banding solutions. Top [(a),(b),(c)]: images for the 95-$R = 0.57$ solution, which consists of linear wormlike micelles. Bottom [(d),(e),(f)]: images for the 95-$R = 0.79$ solution, which consists of branched wormlike micelles.

inner corner upstream of the 90° bend. At a fixed *Wi*, this lip vortex remained unchanged in length and shape over time [Figs. 3(b) and 3(e)]. The critical *Wi* for the transition from no secondary flow to a steady lip vortex is between $Wi = 5.0$ and 7.4 for the 95 mM-$R = 0.55$ solution and between $Wi = 12.5$ and 18.8 for the 25 mM-$R = 1$ solution. As *Wi* was increased beyond these values, the vortex grew in length but remained steady until, upon further increases in *Wi*, both solutions showed a second transition where the inner corner lip vortex became unsteady and fluctuating over time. Figures 3(c) and 3(f) show two streak images for each solution in this regime, in which the two images were taken several seconds apart. There is a clear time dependence of the shape and length of the lip vortices in this regime. The critical *Wi* for the transition to this unsteady lip vortex regime is between $Wi = 39.7$ and 49.6 for the 95 mM-$R = 0.55$ solution and between $Wi = 125.1$ and 150.3 for the 25 mM-$R = 1$ solution. Although the steady lip vortices were also reported in shear-thinning solutions of linear polymers [31], the third regime of unsteady lip vortices has only been reported in wormlike micellar fluids [32]. We note, however, that a recent study in ultra-dilute (as low as 50 ppm) PEO solutions shows possible unsteady flow around a 90° microbend when inertial effects become significant [41]. In the present experiments with wormlike micellar solutions, $Re \ll 1$ for all experiments, and inertial effects are expected to be negligible.

The results from the two shear-banding solutions are shown in Fig. 4. Similar to the non-shear-banding solutions, the flow was stable with no vortex at low *Wi* [Figs. 4(a) and 4(d)]. The critical *Wi* for the first flow transition is also similar to those reported in the non-shear-banding solutions: between $Wi = 6.8$ and 9.1 for the 95 mM-$R = 0.57$ solution and between $Wi = 4.3$ and 6.5 for the 95 mM-$R = 0.79$ solution. However, the second flow regime showed different secondary flow behavior. Apart from the lip vortex that formed at the inner corner, another vortex developed at the outer corner of the bend [Figs. 4(b) and 4(e)]. Moreover, unlike the steady lip vortices formed in the non-shear-banding solutions, here both the inner and outer corner vortices showed noticeable

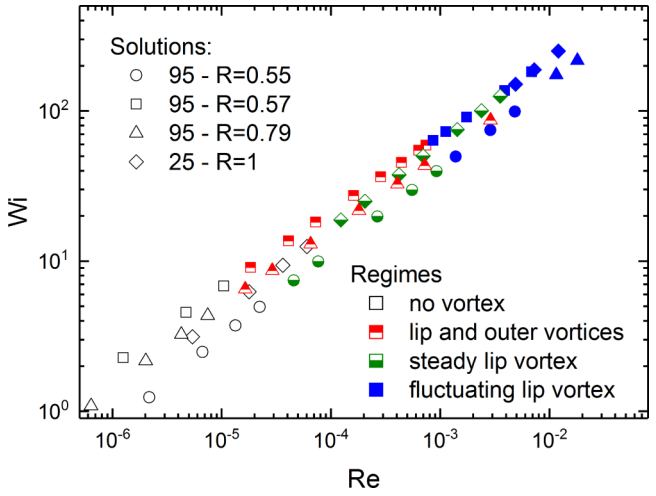

FIG. 5. The flow regimes for each of the four solutions studied on *Wi-Re* coordinates.

temporal fluctuations. In particular, the formation of an outer corner vortex was sporadic, and it disappeared completely at times. Detailed characterization of the vortices (sizes and fluctuations) is available for the 95 mM-$R = 0.79$ solution in the previous study [32]. As *Wi* was further increased, the outer corner vortex no longer formed, and a fluctuating inner corner lip vortex similar to those observed in the non-shear-banding solutions was observed [Figs. 4(c) and 4(f)]. The critical *Wi* for this transition to only an unsteady inner lip vortex is between $Wi = 59.1$ and 63.7 for the 95 mM-$R = 0.57$ solution and between $Wi = 86.8$ and 130.2 for the 95 mM-$R = 0.79$ solution.

Figure 5 summarizes the results from the four wormlike micellar solutions in a *Wi-Re* phase plot. It is clear that the ranges of *Wi* and *Re* accessed in the microbend experiments were comparable among the solutions. In terms of the elasticity number, $El = Wi/Re$, all the data points fall in the range of $El \sim 10^5$ to 10^6. This indicates that the flow transitions occurring in the microbend flow are purely elastic, while inertia plays a minimal role. For each of the four test solutions, we found three distinct flow regimes, with the two transitions between regimes taking place at comparable Weissenberg numbers across the solutions, i.e., a first transition at $Wi \sim 10$ and a second at $Wi \sim 100$. The first and the third flow regimes are similar across all four solutions: at low *Wi* the flows are steady and without any secondary flow, and at very high *Wi* fluctuating lip vortices were present at the inner corner upstream of the microbend. As noted above, the unsteady lip vortex regime seems to be unique to wormlike micellar fluids, as both shear thinning PEO solutions [31] and λ-DNA suspensions [30] showed no fluctuations in the lip vortices formed at comparable *Wi*. On the other hand, the flow behavior in this high *Wi* fluctuating lip vortex regime was consistent across all four test solutions, regardless of rheological characteristics or micelle morphology. The fluctuating lip vortex could be a result of breakage of the wormlike micelle network in strong shear flow. Unlike polymer chains, which are covalently bonded, wormlike micelles are self-assembled by weaker interactions and may break when subjected to strong flows. This is consistent with the observed uniqueness of the fluctuating lip vortex to wormlike micellar solutions. In addition, the breakdown of the micelle network erases the differences in micelle morphology and other characteristics at rest, which could explain the universality of the fluctuating lip vortex across all tested wormlike micellar solutions. Recent simulations by Kalb *et al.* [42] in a cross slot geometry suggests that chain breakage and reformation plays a key role on the formation of a lip vortex in that flow.

Comparing the flow behavior among the four test solutions, first we note the results from the non-shear-banding, linear micelle solution (95 mM-$R = 0.55$), and the shear-banding, branched micelle solution (95 mM-$R = 0.79$) are in quantitative agreement with the previous results for the same solutions in terms of critical conditions [32]. Detailed characterizations of the lip vortex and

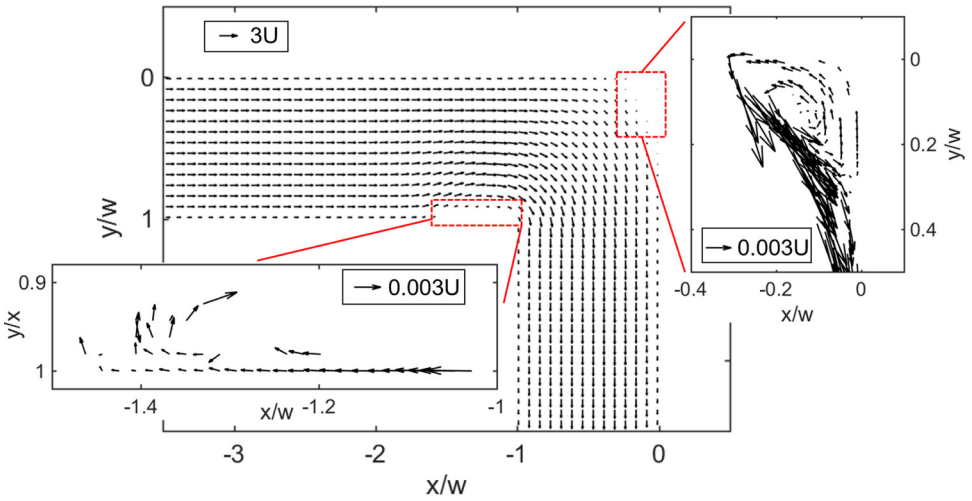

FIG. 6. Velocity vector field for flow of the 95 mM-$R = 0.57$ solution (shear-banding, linear micelles) at volumetric flow rate of $Q = 40\,\mu$L/hr, which corresponds to $Wi = 36.4$ and $Re = 2.8\times10^{-4}$. The reference arrow length is given in terms of the mean flow velocity $U = Q/hw$.

outer corner vortex formation (vortex sizes and fluctuations) are available in the previous study. Although vortex sizes and fluctuation time scales were not quantified in the present study, they appear qualitatively similar to our earlier results. Comparing the two new solutions tested in the present study provides additional insights into the flow behavior of wormlike micellar solution around the microbend. In particular, the flow behaviors observed for the two non-shear-banding solutions versus the two shear-banding solutions were distinctly different, especially in the second flow regime. Conversely, within the two solution pairs, the flow transitions and secondary flow patterns were relatively unaffected by the changes in the morphology of the wormlike micelles (i.e., linear versus branched). Therefore, it appears that the flow behavior in the microbend is determined mainly by the rheological characteristic of shear-banding, rather than by the micelle morphology. Moreover, both the 25 mM-$R = 1$ and the 95 mM-$R = 0.79$ solutions showed apparent shear-thickening regions in steady shear rheology measurements [see Fig. 2(b)]; however, the underlying shear-induced structure formation seems to have little qualitative effect on the flow behavior around the microbend. There are some slight quantitative differences in the critical *Wi* between solutions, and it may be that shear-thickening results in a very modest stabilization of the flow at high *Wi*. However, further experiments are needed to fully resolve the effects, if any, of shear-thickening on this flow.

The PTV protocol was used to further quantify the flow around the microbend. Figure 6 shows the mid-plane velocity vector field of the primary flow of the 95 mM $-$ R $= 0.57$ solution (shear-banding, linear micelles) at $Wi = 36.4$ and $Re = 2.8\times10^{-4}$. Here the x and y positions are nondimensionalized by the channel width w, and the reference arrow length is given in terms of the mean flow velocity $U = Q/hw$, where Q is the volumetric flow rate (here $Q = 40\,\mu$L/hr). The presence of the vortex regions at both the inner and outer corner of the bend effectively focused the primary flow towards the center line of the bend. One result of this flow focusing around the bend is that the effective channel width is decreased at the bend, and the fluid has to accelerate around the bend. This could lead to a higher effective local *Wi* at the bend than the reported *Wi* based on straight channel flow. The flow upstream of the bend is also disturbed by the lip vortex at the inner corner. However, the disturbance does not extend much further upstream than the length of the lip vortex, as the velocity profile across the channel width quickly recovers symmetry about the centerline (see Fig. 7).

The secondary flows within the vortex regions were significantly slower than the primary flow, and only a limited number of particles enter the vortices over short periods of time. Therefore the

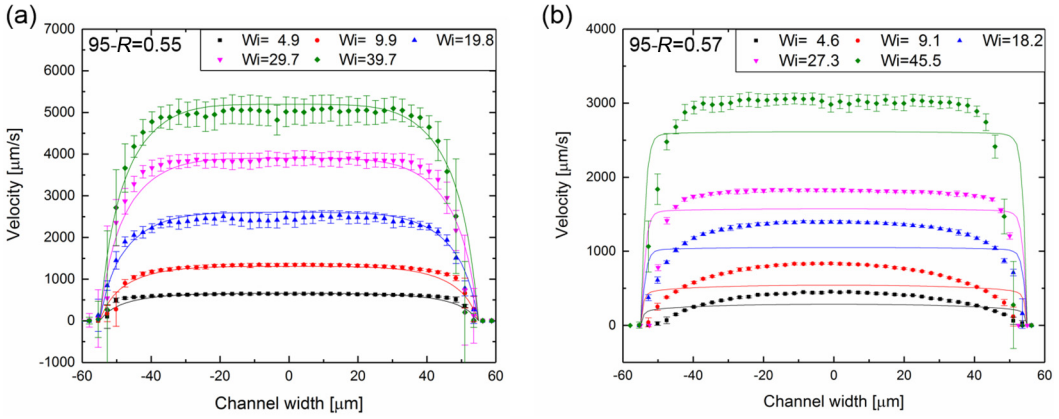

FIG. 7. Comparison of velocity profiles at about 5w upstream of the bend, between (a) non-shear-banding 95-$R = 0.55$ solution and (b) shear-banding 95 mM-R-0.57 solution.

secondary flows were measured separately using lower camera recording speeds, and are plotted in the insets of Fig. 6 with different vector length scaling. Due to the long time averages, the possible fluctuations in the vortices are not captured by the PTV measurement. Nevertheless, the recirculation pattern is clearly shown in both the inner and outer corner vortices, and the fluid velocities within the vortices were found to be almost three orders of magnitude smaller than the primary flow.

To further quantify the fluid flow in the microbend device, we measured the velocity profiles across the channel width upstream of the 90° bend, and compared it with calculated velocity profiles in the rectangular channel for a Carreau fluid. Figure 7 shows the velocity profiles of the two linear micellar solutions with varying *Wi*. The profiles reported here were obtained by averaging over a section of $3 - 7w$ upstream of the bend. Additional measurements were also made much further from the bend at $\sim 30w$ upstream, and no noticeable differences in the velocities were found. The error bars on the data are the standard deviations when the velocity is averaged along the channel. The error becomes larger with increasing *Wi* since the recording frame rate was set higher to reduce motion blur of the particles, which in turn reduces the brightness of the images and therefore the signal-to-noise ratio.

For the two solutions shown in Fig. 7, i.e.,95 mM-$R = 0.55$ and $R = 0.57$, the Carreau model showed good fits to the shear-rate-dependent viscosities across all shear rates measured in the steady shear rheology [Fig. 1(b)]. However, for the two highest Weissenberg numbers shown in Fig. 7, the wall shear rates are likely somewhat higher than the maximum shear rates for which we could obtain rheological data ($\sim 70\,\mathrm{s}^{-1}$), so one may question the extrapolation of the Carreau model to these conditions. With this caveat in mind, a theoretical velocity profile in a rectangular channel can be calculated using the parameters from the Carreau model fit (in Table I) in combination with the Cauchy momentum equation:

$$\frac{\Delta P}{L} + \frac{\partial}{\partial y}\left(\eta(\dot{\gamma})\frac{\partial v_x}{\partial y}\right) + \frac{\partial}{\partial z}\left(\eta(\dot{\gamma})\frac{\partial v_x}{\partial z}\right) = 0. \tag{2}$$

Here x denotes the flow direction and the yz plane is the rectangular channel cross-section. The shear rate here was calculated by $\dot{\gamma}(y,z) = \sqrt{\dot{\gamma}_{xy}^2 + \dot{\gamma}_{xz}^2} = \sqrt{(\partial v_x/\partial y)^2 + (\partial v_x/\partial z)^2}$, $\eta(\dot{\gamma})$ was then calculated using Eq. (1). The resulting partial differential equation (PDE) was solved numerically using Matlab PDE solver with no slip boundary conditions at the channel walls. For comparison with the experimental conditions, the value of the pressure drop $\Delta P/L$ was solved such that the resulting flow velocity $v_x(y,z)$ integrates to a given volumetric flow rate. The calculated velocity profiles at the channel mid-plane are plotted in Fig. 7 to compare with the experimental velocimetry results.

In the 95 mM-R = 0.55 solution (non-shear-banding, linear micelles), the experimental profiles and the calculations based on the Carreau model are in good agreement. On the other hand, the 95 mM-$R = 0.57$ solution, which is shear-banding, shows significant deviations from the Carreau model prediction at moderate *Wi*. The experimentally measured fluid velocities were higher near the center of the channel and lower near the channel walls. The observed deviation from the Carreau predictions is reminiscent of a "jetting" regime observed in wormlike micelle solutions in straight rectangular channels [43,44]. A recent study by Salipante *et al.* [44] attributed the "jetting" regime to the nonmonotonic stress curve in the shear-banding solutions, which is not properly captured when using the Carreau model to fit the apparent shear-dependent viscosity. Instead, these authors recover the jetting regime in simulations using a three-dimensional (3D) Johnson-Segalman model. In the present study, the range of *Wi* over which the disagreement with the Carreau predictions is observed is comparable to (but does not match precisely) the *Wi* range of the second flow regime in the microbend. This flow regime, characterized by both an inner lip vortex and an outer corner vortex, is only observed in the shear-banding fluids, and could therefore be correlated to the occurrence of the shear-banding induced "jetting" in the straight channel before entering the bend. On the other hand, Haward *et al.* [43] observed "jets" in channels with non-shear-banding solutions, suggesting that the channel flows of even shear-thinning wormlike micelle solutions are not well captured by the Carreau model under all conditions. We note that both Salipante and coworkers and Haward and coworkers reported jetting in channels with aspect ratios greater than 5, whereas the aspect ratio in the present study is 2.

V. CONCLUSIONS

The flow of wormlike micellar solutions around a 90° sharp microbend was studied using rheometry, flow visualization, and velocimetry. By carefully choosing the composition of the test solutions, we examined four wormlike micelle solutions in similar ranges of *Wi* and *Re*. These solutions allowed us to access all four combinations of linear or branched micelles and shear-banding or non-shear-banding solutions. When comparing the two shear-banding solutions with the two non-shear-banding ones, the secondary flow pattern showed distinct differences at about $10 < Wi < 100$: a steady lip vortex was formed at the inner corner of the microbend in the non-shear-banding solutions, while a lip (inner corner) vortex and an outer corner vortex were formed in the shear-banding solutions. On the other hand, when comparing the solutions with similar rheological characteristics but different micelle morphology (linear versus branched), no significant difference in the flow behavior was observed. We therefore conclude that shear-banding of the wormlike micellar solution plays a central role in determining the secondary flow behavior around the microbend, while the effect of micelle morphology is minimal. From velocity field measurements, the shear-banding effect could be correlated to the development of a "jetting" flow regime upstream of the bend, which has been attributed to the nonmonotonic stress–shear rate relationship in shear-banding wormlike micellar solutions.

ACKNOWLEDGMENTS

The authors gratefully acknowledge the financial support of this work by the National Science Foundation through Award No. NSF CBET 1335653. The authors also gratefully acknowledge Malvern Instruments for the loan of the Malvern Gemini rheometer.

[1] L. E. Rodd, J. J. Cooper-White, D. V. Boger, and G. H. McKinley, Role of the elasticity number in the entry flow of dilute polymer solutions in micro-fabricated contraction geometries, J. Non-Newton. Fluid Mech. **143**, 170 (2007).

[2] L. E. Rodd, T. P. Scott, D. V. Boger, J. J. Cooper-White, and G. H. McKinley, The inertio-elastic planar entry flow of low-viscosity elastic fluids in micro-fabricated geometries, J. Non-Newton. Fluid Mech. **129**, 1 (2005).

[3] S. Gulati, S. J. Muller, and D. Liepmann, Direct measurements of viscoelastic flows of DNA in a 2:1 abrupt planar micro-contraction, J. Non-Newton. Fluid Mech. **155**, 51 (2008).
[4] S. J. Haward, Z. Li, D. Lighter, B. Thomas, J. A. Odell, and X. F. Yuan, Flow of dilute to semi-dilute polystyrene solutions through a benchmark 8:1 planar abrupt micro-contraction, J. Non-Newton. Fluid Mech. **165**, 1654 (2010).
[5] A. Lanzaro and X. F. Yuan, Effects of contraction ratio on non-linear dynamics of semi-dilute, highly polydisperse PAAm solutions in microfluidics, J. Non-Newton. Fluid Mech. **166**, 1064 (2011).
[6] Z. Li, X. F. Yuan, S. J. Haward, J. A. Odell, and S. Yeates, Non-linear dynamics of semi-dilute polydisperse polymer solutions in microfluidics: Effects of flow geometry, Rheol. Acta **50**, 277 (2011).
[7] M. S. N. Oliveira, L. E. Rodd, G. H. McKinley, and M. A. Alves, Simulations of extensional flow in microrheometric devices, Microfluid. Nanofluidics **5**, 809 (2008).
[8] S. C. Omowunmi and X. F. Yuan, Modelling the three-dimensional flow of a semi-dilute polymer solution in microfluidics-on the effect of aspect ratio, Rheol. Acta **49**, 585 (2010).
[9] T. J. Ober, S. J. Haward, C. J. Pipe, J. Soulages, and G. H. McKinley, Microfluidic extensional rheometry using a hyperbolic contraction geometry, Rheol. Acta **52**, 529 (2013).
[10] M. R. Stukan, E. S. Boek, J. T. Padding, W. J. Briels, and J. P. Crawshaw, Flow of wormlike micelles in an expansion-contraction geometry, Soft Matter **4**, 870 (2008).
[11] M. R. Stukan, E. S. Boek, J. T. Padding, and J. P. Crawshaw, Influence of system size and solvent flow on the distribution of wormlike micelles in a contraction-expansion geometry, Eur. Phys. J. E **26**, 63 (2008).
[12] H. R. Tamaddon Jahromi, M. F. Webster, J. P. Aguayo, and O. Manero, Numerical investigation of transient contraction flows for worm-like micellar systems using Bautista–Manero models, J. Non-Newton. Fluid Mech. **166**, 102 (2011).
[13] P. E. Arratia, C. C. Thomas, J. Diorio, and J. P. Gollub, Elastic Instabilities of Polymer Solutions in Cross-Channel Flow, Phys. Rev. Lett. **96**, 144502 (2006).
[14] P. C. Sousa, F. T. Pinho, M. S. N. Oliveira, and M. A. Alves, Purely elastic flow instabilities in microscale cross-slot devices, Soft Matter **11**, 8856 (2015).
[15] S. J. Haward and G. H. McKinley, Instabilities in stagnation point flows of polymer solutions, Phys. Fluids **25**, 083104 (2013).
[16] F. A. Cruz, R. J. Poole, A. M. Afonso, F. T. Pinho, P. J. Oliveira, and M. A. Alves, Influence of channel aspect ratio on the onset of purely-elastic flow instabilities in three-dimensional planar cross-slots, J. Non-Newton. Fluid Mech. **227**, 65 (2016).
[17] S. J. Haward, G. H. Mckinley, and A. Q. Shen, Elastic instabilities in planar elongational flow of monodisperse polymer solutions, Sci. Rep. **6**, 33029 (2016).
[18] J. A. Pathak and S. D. Hudson, Rheo-optics of equilibrium polymer solutions: Wormlike micelles in elongational flow in a microfluidic cross-slot, Macromolecules **39**, 8782 (2006).
[19] N. Dubash, P. Cheung, and A. Q. Shen, Elastic instabilities in a microfluidic cross-slot flow of wormlike micellar solutions, Soft Matter **8**, 5847 (2012).
[20] S. J. Haward and G. H. McKinley, Stagnation point flow of wormlike micellar solutions in a microfluidic cross-slot device: Effects of surfactant concentration and ionic environment, Phys. Rev. E **85**, 031502 (2012).
[21] S. J. Haward, T. J. Ober, M. S. N. Oliveira, M. A. Alves, and G. H. McKinley, Extensional rheology and elastic instabilities of a wormlike micellar solution in a microfluidic cross-slot device, Soft Matter **8**, 536 (2012).
[22] J. Zilz, R. J. Poole, M. A. Alves, D. Bartolo, B. Levaché, and A. Lindner, Geometric scaling of a purely elastic flow instability in serpentine channels, J. Fluid Mech. **712**, 203 (2012).
[23] J. A. Pathak, D. Ross, and K. B. Migler, Elastic flow instability, curved streamlines, and mixing in microfluidic flows, Phys. Fluids **16**, 4028 (2004).
[24] R. J. Poole, A. Lindner, and M. A. Alves, Viscoelastic secondary flows in serpentine channels, J. Non-Newton. Fluid Mech. **201**, 10 (2013).
[25] F.-C. Li, H. Kinoshita, X.-B. Li, M. Oishi, T. Fujii, and M. Oshima, Creation of very-low-Reynolds-number chaotic fluid motions in microchannels using viscoelastic surfactant solution, Exp. Therm. Fluid Sci. **34**, 20 (2010).

[26] R. J. Poole, M. Alfateh, and A. P. Gauntlett, Bifurcation in a T-channel junction: Effects of aspect ratio and shear-thinning, Chem. Eng. Sci. **104**, 839 (2013).
[27] M. G. N. Perera and K. Walters, Long-range memory effects in flows involving abrupt changes in geometry. Part II: The expansion/ contraction/ expansion problem, J. Non-Newton. Fluid Mech. **2**, 191 (1977).
[28] S. Chono and Y. Iemoto, Numerical simulation of viscoelastic flow in two-dimensional L-shaped channels, J. Rheol. (NY) **36**, 335 (1992).
[29] T. Cochrane, K. Walters, and M. F. Webster, Newtonian and non-Newtonian flow near a re-entrant corner, J. Non-Newton. Fluid Mech. **10**, 95 (1982).
[30] S. Gulati, D. Liepmann, and S. J. Muller, Elastic secondary flows of semidilute DNA solutions in abrupt 90° microbends, Phys. Rev. E **78**, 036314 (2008).
[31] S. Gulati, C. S. Dutcher, D. Liepmann, and S. J. Muller, Elastic secondary flows in sharp 90 degree micro-bends: A comparison of PEO and DNA solutions, J. Rheol. (NY) **54**, 375 (2010).
[32] M. Y. Hwang, H. Mohammadigoushki, and S. J. Muller, Flow of viscoelastic fluids around a sharp microfluidic bend: Role of wormlike micellar structure, Phys. Rev. Fluids **2**, 43303 (2017).
[33] X. Xiao, V. F. Geyer, H. Bowne-Anderson, J. Howard, and I. F. Sbalzarini, Automatic optimal filament segmentation with sub-pixel accuracy using generalized linear models and B-spline level-sets, Med. Image Anal. **32**, 157 (2016).
[34] C. D. Meinhart, S. T. Wereley, and M. H. B. Gray, Volume illumination for two-dimensional particle image velocimetry, Meas. Sci. Technol. **11**, 809 (2000).
[35] See Supplemental Material at http://link.aps.org/supplemental/10.1103/PhysRevFluids.3.093301 for additional information about the experiements and the analysis.
[36] J. F. Berret, J. Appell, and G. Porte, Linear rheology of entangled wormlike micelles, Langmuir **9**, 2851 (1993).
[37] E. Cappelaere and R. Cressely, Shear banding structure in viscoelastic micellar solutions, Colloid Polym. Sci. **275**, 407 (1997).
[38] C. Oelschlaeger, M. Schopferer, F. Scheffold, and N. Willenbacher, Linear-to-branched micelles transition: A rheometry and diffusing wave spectroscopy (DWS) study, Langmuir **25**, 716 (2009).
[39] D. Gaudino, R. Pasquino, and N. Grizzuti, Adding salt to a surfactant solution: Linear rheological response of the resulting morphologies, J. Rheol. (NY) **59**, 1363 (2015).
[40] L. Ziserman, L. Abezgauz, O. Ramon, S. R. Raghavan, and D. Danino, Origins of the viscosity peak in wormlike micellar solutions. 1. mixed catanionic surfactants. A cryo-transmission electron microscopy study, Langmuir **25**, 10483 (2009).
[41] J. Kim, S. O. Hong, T. S. Shim, and J. M. Kim, Inertio-elastic flow instabilities in a 90° bent microchannel, Soft Matter **13**, 5656 (2017).
[42] A. Kalb, U. L. A. Villasmil, and M. Cromer, Role of chain scission in cross-slot flow of wormlike micellar solutions, Phys. Rev. Fluids **2**, 071301(R) (2017).
[43] S. J. Haward, F. J. Galindo-Rosales, P. Ballesta, and M. A. Alves, Spatiotemporal flow instabilities of wormlike micellar solutions in rectangular microchannels, Appl. Phys. Lett. **104**, 124101 (2014).
[44] P. F. Salipante, C. A. E. Little, and S. D. Hudson, Jetting of a shear banding fluid in rectangular ducts, Phys. Rev. Fluids **2**, 33302 (2017).